



Thermal stability of electrodeposited nanostructured high-entropy alloys

Michel J.R. Haché*, Yu Zou*, Uwe Erb

Department of Materials Science and Engineering, University of Toronto, 184 College St., Toronto, ON M5S 3E4, Canada



ARTICLE INFO

Keywords:

High-entropy alloy
Nanostructured
Thermal stability
Nanoglass
Electrodeposition

ABSTRACT

Over the past decade, the study of nanostructured high-entropy alloys (HEAs) has attracted great attention due to their high strength (grain boundary hardening) and improved thermal stability over conventional nanostructured metals and alloys. However, a lingering issue yet to be resolved by these studies is that of commercial viability; the synthesis processes used to date are costly, not easily scalable, and energy intensive. This work examines the thermal stability and mechanical properties of electrodeposited nanostructured HEAs, towards establishing a cost-effective and versatile synthesis route to commercialize this underutilized material class. Nanocrystalline, amorphous, and nanoglass alloys of NiFeCoW, NiFeCoMo, and NiFeCoMoW were systematically characterized to assess the stability of their structure and mechanical properties, compared against conventional nanocrystalline materials and HEA counterparts. The structural stability of these electrodeposited HEAs was shown to improve with increasing number of elements, from a peak temperature for grain growth of ~270 °C in pure nanocrystalline Ni, to ~500 °C in electrodeposited HEAs, corresponding to a near doubling of the activation energy for grain growth from 1.3 eV (Ni) to a maximum of 3.1 eV (NiFeCoW). This improved stability was matched with a 60 % increase in hardness after annealing to the point of nanograins nucleation (~500 °C), to a maximum hardness of ~8.4 GPa. Such hardening trends followed an extrinsic inverse-to-regular Hall-Petch relationship, where the inverse regime was largely dominated by grain boundary relaxation and nanoglass structural breakdown. With these results, we have established electrodeposition as a promising candidate route for fabricating nanostructured HEAs for applications at elevated temperatures.

1. Introduction

Grain boundary strengthening is a longstanding method that has been used to improve the strength and/or hardness of metallic materials through an increase in interfacial free volume (or grain boundary volume fraction), microstructural defects which act to impede dislocation motion. The Hall-Petch (HP) [1,2] relationship is classically used to describe this effect:

$$\sigma_y = \sigma_o + k_y d^{-\frac{1}{2}} \quad (1)$$

where σ_y is the yield strength, σ_o the overall resistance of the lattice to dislocation motion, and k_y a constant related to the relative hardening contribution of grain boundaries [3]. Naturally, this size-effect is amplified in nanocrystalline materials, where the volume fraction of atoms at grain boundaries begins to approach that of atoms located in the grain interiors. However, since their inception in the 1980's, metallurgical nanomaterials (one of the parent sets of nanocrystalline materials) have long suffered from poor stability, as grains tend to

coarsen when exposed to high, and even moderate temperatures.

Recently, the concept of mixing multiple elements in roughly equal proportions has been adopted to overcome constraints that exist in traditional metallurgical materials. These so-called high-entropy alloys (HEAs, alloys made up of 4–5 or more elements, each with compositions in the range 5–35 at.%) [4,5] have since gained considerable popularity in the past two decades [6–8]. One critical avenue of this work has been in the development of nanocrystalline HEAs, towards improved mechanical performance and thermal stability. To this end, much of the focus on this topic has centered on 3d transition and refractory HEAs made by solid-state (e.g., high-pressure torsion [5], equal-channel angular pressing [9], ball milling [10]) and vapour-state (e.g., DC magnetron co-sputtering [11,12], inert gas condensation [13]) processing methods to achieve nanocrystalline structures [14]. These studies have reported improvements in thermal stability and mechanical properties in alloys such as NbTaMoW [15,16], CoCrFeMnNi [9,13,17–20], HfNbTiZr [21], and Ni-ZrNbMoTa [22].

While providing great advancement to the field, most of these studies

* Corresponding authors.

E-mail addresses: michel.hache@mail.utoronto.ca (M.J.R. Haché), mse.zou@utoronto.ca (Y. Zou).

have thus far lacked a fundamental consideration that has plagued much of HEA literature: application-ready fabrication processes. Despite their excellent properties, HEAs generally hold a high material cost, owing to the fraction of expensive alloying elements needed in their makeup (for instance, Co, Cr, Ni, Mn in the Cantor alloy). To combat this high material cost, and therefore make HEAs a more commercially practicable option, it is critical to have a viable low-cost synthesis route. Considering those vapour- and solid-state techniques used to date, their drawback in this regard is their generally high energy input, low yield, or their necessity for controlled atmosphere [23–26].

Looking to other routes for the synthesis of nanostructured materials, a large commercial success has been in electrodeposition; a highly scalable, low-cost, and low-energy input process that can be readily applied to existing infrastructure [27–29]. Indeed, since 2019 the exploration of electrodeposited HEAs has rapidly expanded, with over 25 publications to date. These attempts have largely focused on applications in corrosion [30–33], catalysis [34], and magnetism [32,35], and have thus far produced coatings of generally poor quality (e.g., cracking, massive segregation, impurity uptake, or low thickness). One of few concerted efforts in this field has been the sequential works of the authors of this study, who, using a graduated approach, built an incremental base of understanding in the electrodeposition of NiFeCr [36,37], NiFeCo [37], and finally NiFeCo-(Mo/W) [38] nanostructured and amorphous medium-entropy alloys (MEAs) and HEAs. The current work builds on the framework established in Refs. [37, 38] to systematically assess the feasibility of using electrodeposition to produce nanocrystalline HEAs with greater thermal stability than their conventional pure metal and alloy counterparts. In doing so, we hope to establish electrodeposition as a method that accelerates and expands commercial adoption of both metallurgical nanomaterials and HEAs.

2. Experimental

Near-equimolar alloys of NiFeCoW, NiFeCoMo, and NiFeCoMoW were electrodeposited onto 2×2 cm Cu substrates via the electrodeposition processes outlined in Ref. [38], reproduced in detail in Section 1 of Supplementary Materials. Scanning electron microscopy (SEM, Hitachi SU3500) was coupled with energy-dispersive X-ray spectroscopy (EDS, Oxford Instruments) to determine the composition of each alloy. Scanning/transmission electron microscopy (S/TEM, Hitachi HF3300) was carried out on each of the as-deposited samples, which were prepared via focused-ion beam (FIB, Hitachi MB5000). Isochronal annealing of the samples was conducted in the temperature range 200–800 °C for 1 h, followed immediately by quenching in room temperature water. Low-temperature annealing (<500 °C) was performed in a salt bath furnace containing a mixture of NaNO₂ and KNO₃. Samples were sealed in stainless steel bags for protection from the salt environment. High-temperature annealing (>500 °C) was performed in a tube furnace, where samples were sealed under vacuum (0.01 mbar) in quartz tubes prior to annealing to limit surface oxidation. Although this technique effectively protected the bulk of the coatings, thin oxide layers (up to 200 nm thick) often formed at the outer surfaces. Planar ion-milling (Hitachi IM4000I/II) was then used to remove remaining oxides prior to any subsequent characterization.

Room temperature planar X-ray diffraction (XRD) measurements (Bruker D8 Discover) of annealed samples were made using a Cu-K_α X-ray source ($\lambda = 0.154$ nm) at locations near the center of the samples, where the deposits were most uniform. Grain size measurements were made from these datasets using the Scherrer approach [39]:

$$d = \frac{K\lambda}{B_{size} \cos\theta} \quad (2)$$

where K is a constant (typically 0.9), λ is the wavelength of the incident X-ray beam, B_{size} is the grain size contribution to the full-width at half the maximum (FWHM) of the selected peak, and θ is the Bragg angle.

In preparation for imaging and mechanical testing, the annealed samples were sectioned using a low-speed diamond abrasive wheel, mounted in epoxy via vacuum impregnation, and ground and polished down to a 20 nm colloidal silica abrasive. The polished deposits were subjected to instrumented nanoindentation (iMicro, KLA-Tensor) using a diamond Berkovic tip (Synton), which was calibrated before each test using a fused Si standard. The ISO14577 constant loading rate indentation method [40] was used for all samples, with a maximum load of 10 mN, loading rate of 1 mN/s, and hold time of 15 s. Indents were located along the mid-line of the coating cross-sections in order to eliminate substrate and surface effects. A minimum of 25 indents were performed for each sample. Indent spacings followed ISO14577 guidelines ($>3 \times$ indent diagonals) [40]. Static strain-rate-sensitivity (SRS) tests were then performed using continuous stiffness measurements (CSM) under constant strain rates of [0.01, 0.05, 0.1, 0.5, 1] s⁻¹, up to a maximum depth of 200 nm (to eliminate any indentation size effects [41]). Average values were calculated from 10 tests performed at each strain rate. Activation volumes (V) were then calculated from the relationship [42,43],

$$V = 3\sqrt{3}kT \left(\frac{\partial \ln \dot{\epsilon}}{\partial H} \right) \quad (3)$$

where k is Boltzmann's constant, T the testing temperature, $\dot{\epsilon}$ the strain rate, and H the hardness.

Synchrotron XRD measurements were performed at the Brockhouse high-energy wiggler beamline (WHE) at the Canadian Light Source (CLS) in Saskatchewan, Canada. GSAS-II software was used to process all data from these experiments, processing the raw diffraction patterns to generate diffraction profiles, and from these generating pair distributions functions (PDFs). PDFs were generated from the synchrotron XRD data by applying the sine Fourier transform:

$$G(r) = 4\pi(\rho(r) - \rho_0) = \frac{2}{\pi} \int_0^\infty Q[S(Q) - 1] \sin(Qr) dQ \quad (4)$$

where $\rho(r)$ is the microscopic pair density, ρ_0 the average number density, Q the magnitude of the scattering vector, and $S(Q)$ the normalized scattering intensity [44]. For elastic scattering, Q is calculated as:

$$Q = \frac{4\pi \sin\theta}{\lambda} \quad (5)$$

From these, radial distribution functions (RDFs) were generated for peak fitting and analysis of bond distances and lattice disorder, through the relationship [45]:

$$RDF = 4\pi r^2 \rho(r) = 4\pi r^2 \rho_o + r^* G(r) \quad (6)$$

Differential scanning calorimetry (DSC) was used to assess the structural thermal stability of the deposits. Samples were scanned at heating rates of 5, 10, and 20 °C·min⁻¹ in the temperature range 300–800 °C (Netzsch 449 F3 Jupiter HV STA). To prevent oxidation, the system was evacuated and purged with 99.999 % Ar at a flow rate of 50 mL·min⁻¹. Exothermic peaks corresponding to grain growth or phase decomposition were analyzed, and peak temperatures (T_p) extracted from these datasets. The activation energy for grain growth (Q) was determined through the modified Kissinger analysis [46]:

$$\ln\left(\frac{b}{T_p}\right) = \frac{Q}{kT_p} + C \quad (7)$$

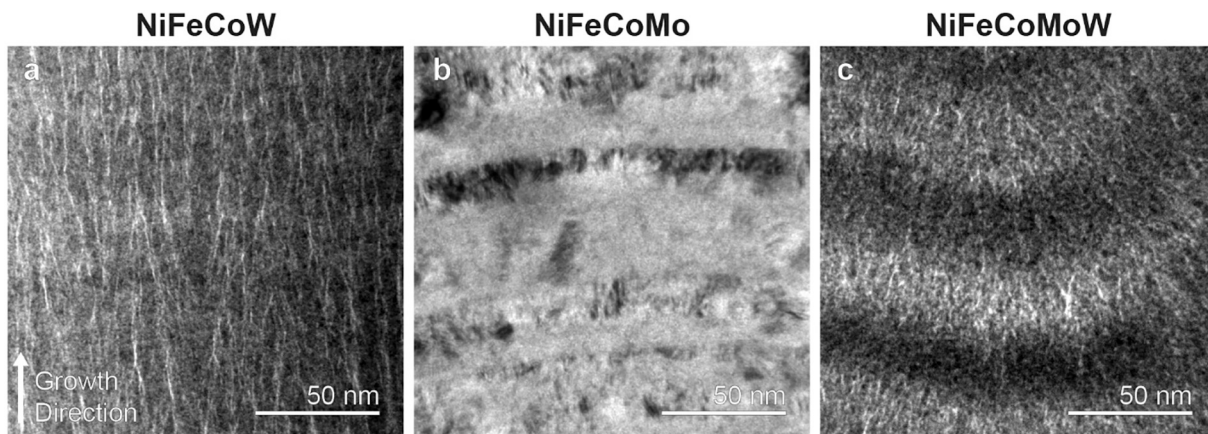
where b is the heating rate, k Boltzmann's constant, and C a constant.

To employ synchrotron XRD and differential scanning calorimetry, a method of removing the substrate material from the electrodeposited HEAs was devised. The original Cu substrate from [38] was replaced with 1 cm wide Cu tape, which was masked with 3M™ high-adhesion tape, leaving an exposed area of approximately 0.9×1.5 cm². Electrodeposition was then carried out using identical procedure, bath

Table 1

Compositions (at.%) and characteristics of the electrodeposited HEAs in this study.

Alloy	Composition (at.%)					Thickness (μm)	Dominant phase	Grain size, TEM (nm)
	Ni	Fe	Co	Mo	W			
NiFeCoW	18	34	23	—	25	31	Amorphous	—
NiFeCoMo	21	27	29	23	—	44	Amorphous/ Nanocrystalline	8
NiFeCoMoW	30	23	22	13	13	40	Amorphous	—

**Fig. 1.** As-deposited microstructures of HEA electrodeposits: (a) NiFeCoW, (b) NiFeCoMo, and (c) NiFeCoMoW (adapted from [38] with permission from Elsevier).

composition, and electroplating variables to those used to synthesize equimolar NiFeCoW, NiFeCoMo, and NiFeCoMoW [38]. The deposits were then mechanically stripped from the Cu tape, forming a flaky powder. The compositions of these powders were determined via EDS, which revealed slight deviations from their nominal values in the rigid Cu-coupon deposits analyzed throughout this work. These differences are listed in Supplementary Table S2, the most notable being the Ni content.

3. Results and discussion

Three electrodeposited HEAs made up of NiFeCoW, NiFeCoMo, and NiFeCoMoW were analyzed to assess their performance with regards to thermal stability of structure and mechanical properties. These alloys, whose synthesis and as-deposited properties were earlier discussed at length in ref. [38], have compositions and microstructures shown in Table 1 and Fig. 1, respectively.

Alloys containing W each have what was earlier postulated [38] to be a nanoglass (NG) structure, elongated in the growth direction of the deposits. NiFeCoMo has a unique structure of laminated layers of amorphous and nanocrystalline (8 nm grain size) phases in roughly equal area fractions.

A notable part of the microstructure that may affect the properties of these electrodeposited HEAs is banding, which typically resulted from segregation of Ni with W and Fe with Mo (see Fig. 1). In the instance of NiFeCoMo, such segregation was severe enough to result in a coupled structural banding effect, with Ni-rich regions taking on a nanocrystalline structure, and Mo-rich regions an amorphous structure (Fig. 1b). Band thickness measurements performed on cross-sectional SEM and TEM micrographs are summarized in Table 2. Overall, measurements

from SEM micrographs resulting in greater band thickness, as the contrast was primarily dominated by topographical differences between the bands, resulting from selective etching of layers of varying composition when exposed to colloidal silica polishing medium (20 nm particle size). Band thickness measured by TEM was much smaller, on the order of tens of nanometers, corresponding to deposition times of ~1–9 s per band.

3.1. Isochronal annealing

Isochronal annealing of the electrodeposited HEAs was performed in the temperature range 200–800 °C to provide a general assessment of their thermal stability. Planar XRD profiles of the annealed samples in Fig. 2 show the structural evolution as a function of annealing temperature. NiFeCoW (Fig. 2a) had a stable amorphous structure below 500 °C, at which point nanograins nucleation commenced, forming a mixed crystalline-amorphous structure. The rightward shift of the emerging crystalline peak as compared to the amorphous profile points to a BCC α -Fe structure, following what has been previously observed in annealed amorphous FeW electrodeposits [47]. This evolution to a nanocrystalline structure continued up to 600 °C with more pronounced crystalline phase formation in the form of an FCC γ -Ni and W-rich BCC phase. At 700 °C, significant phase decomposition developed in the form of both metallic and intermetallic compounds relating to impurities and surface oxidation. Although the sample surfaces were ion-milled to remove the thin layer of oxidized material (~200 nm thick), cracks that formed in the deposits as a result of annealing allowed oxidation to penetrate deeper into the material as shown in Fig. 3. As such, oxides such as $\text{Fe}(\text{WO}_4)$ and $\text{W}_3\text{M}_3\text{O}$ (where M is Ni, Fe, or Co) appear in the XRD profiles. Past reports by Mulone et al. [47,48] on FeW have also

Table 2

Band thickness measured by SEM and TEM, and approximate deposition time/band from TEM measurements.

Alloy	SEM band thickness (nm)	TEM band thickness (nm)	Deposition time/band (s)
NiFeCoW	159 ± 10	38 ± 2	9
NiFeCoMo	85 ± 2	18 ± 9	1
NiFeCoMoW	97 ± 2	29 ± 2	3

indicated that upon phase decomposition at 800 °C, carbide ($\text{Fe}_3\text{W}_3\text{C}$ and $\text{Fe}_6\text{W}_6\text{C}$), oxide (FeWO_4), and intermetallic (Fe_2W) phases develop in addition to crystalline metallic phases, many of which overlap with the phases indexed in Fig. 2a.

Interestingly, the XRD profile for the as-deposited amorphous/nanocrystalline form of NiFeCoMo only revealed the amorphous nature of the alloy, as no separate nanocrystalline phase (such as seen in Fig. 1b) could be decoupled from the single broad peak. The pseudo-amorphous NiFeCoMo structure began to decompose at 400 °C (Fig. 2b) into what is likely to be overlapping FCC phases, corresponding to growth of one of either its amorphous or nanocrystalline banded regions. Significant phase decomposition emerged at 500 °C (α -Fe), though the broad amorphous peak remained until 600 °C, where oxidation and other phase transformations became more prevalent and grain coarsening was apparent (Supplementary Fig. S1).

NiFeCoMoW behaved more alike to NiFeCoW, as nanograins nucleation began at 500 °C, forming nanocrystalline α -Fe within its amorphous matrix. Significant phase decomposition then took place at 600 °C, though it retained some of its original near-amorphous character before complete decomposition and grain growth at 700 °C (where oxidation and other phase formations also became more prevalent – Supplementary Fig. S2).

The components of phase decomposition and grain growth that were observed in the planar XRD profiles in Fig. 2 are quantitatively summarized through the plots in Fig. 4a, c, and e, which reveal the grain size of each phase (measured from X-ray peak broadening and SEM micrographs) as a function of annealing temperature. These trends were coupled with instrumented nanoindentation testing to relate the evolution of hardness and elastic modulus with the structure of the deposits at each annealing temperature (Fig. 4b, d, and f).

In NiFeCoW, the hardness and elastic modulus initially increased with increasing temperature, up to 400 °C, while no observable grain growth took place in this low-temperature regime. At 500 °C nanograins nucleation began, forming a mixed amorphous and nanocrystalline BCC structure, while hardness and elastic modulus continued to increase. Further increase in temperature to 600 °C resulted in slight grain growth and additional phase decomposition, whose combined effect led the hardness to plateau at ~ 8.4 GPa, while the elastic modulus continued to increase as the crystallinity increased with annealing temperature. The overall trend in elastic modulus followed the expected model of Zhou et al. [49], which was also observed in the NiFeCr and NiFeCo MEA electrodeposits [37]. At 700–800 °C, more noticeable decomposition and grain growth occurred, resulting in an abrupt decrease in hardness.

Nanoindentation testing of the annealed NiFeCoMo samples (Fig. 4d) revealed a similar trend to NiFeCoW, showing increasing hardness with increasing annealing temperature, up to a peak at 600 °C. In this temperature range the “grain size” of the amorphous phase remained nearly constant (Fig. 4c), while phase decomposition and grain growth of the secondary FCC phase began at 400 °C. At this point, the elastic modulus experienced a sudden rise, as was expected during crystallization. More significant phase decomposition occurred at 600 °C, where Mo-rich clusters (which likely take on a BCC structure) began to form. Further annealing to 700 °C led to significant grain growth and further phase decomposition, resulting in a ~ 2 GPa drop in hardness, while the elastic modulus experienced a second jump up to a maximum of 189 ± 21 GPa.

The hardness trends in NiFeCoMoW were nearly identical to those of the 4-element HEAs; hardness increased almost linearly with increasing annealing temperature, up to 500 °C. In this temperature regime, there was little or no noticeable grain growth, as shown in Fig. 4e. As relaxation and nanograins nucleation began, the elastic modulus increased with annealing temperature, again following the trends observed in NiFeCoW and NiFeCoMo. The hardness then decreased at 700 °C and 800 °C, corresponding to grain coarsening.

3.2. Thermal stability comparison

A test of the hypotheses of improved mechanical performance and thermal stability in electrodeposited nanocrystalline HEAs over their coarse-grained and conventional counterparts (e.g., pure metal, dilute alloys) necessitates an overall comparison of the electrodeposited alloys studied here. Though literature that offers a direct comparison with the annealing data acquired in this study is limited, a few key cases exist that offer a test of the hypotheses: electrodeposited Ni [50,51], NiCo [52], and NiFeCo [37], and NiFeCoCrMn [18] made by high-pressure torsion (HPT). Each of these exemplars were first fabricated with a homogeneous nanocrystalline structure and then annealed for 1 h at varying temperatures to uncover the thermal stability of grain size and hardness. These trends are shown in Fig. 5 along with those from the electrodeposited HEAs from this study.

Improved grain size stability with increasing alloy complexity is immediately seen in Fig. 5a, wherein the critical temperature for grain growth incrementally increases ~ 50 °C with each added element from Ni (~ 200 °C) to NiCo (~ 250 °C), and then to NiFeCo (~ 300 °C). It is important to note that onset temperatures for grain growth would, on the whole, be expected to be lower than these peak temperatures, as reported by Klement et al. [53] in Ni, which undergoes some localized growth via subgrain coalescence at ~ 100 °C, and later confirmed by Natter et al. [50]. The addition of a 4th element of Mo or W further increases that stability up to ~ 500 °C, but no improvement is observed in the 5-element NiFeCoMoW over its 4-element subsets. However, these 4–5 element HEAs do show a marked improvement over NiFeCoCrMn made by HPT, which experienced grain growth at temperatures beyond 400 °C. This is likely due to the addition of refractory elements to the 3d transition metal base of NiFeCo, as in their pure state W and Mo have comparatively high melting temperatures. However, these large increments in annealing temperature make it difficult to reach a definite conclusion on the comparative thermal stability of these alloys. A more detailed analysis of their thermal stability was thus carried out in Section 3.3.

The trends in the stability of hardness in Fig. 5b are altogether different from that of grain size. Each alloy experiences an increase in hardness at relatively low annealing temperatures (<300 °C) before a drop-off at temperatures corresponding to massive grain growth, indicative of regular HP behaviour. However, this hardening effect appears to be amplified in the electrodeposited 4- and 5-element HEAs, as they experience a near 60 % increase in hardness from the as-deposited state to the samples annealed at 600 °C, compared to a maximum increase of ~ 10 % across all other metals and alloys. Unlike the others, they also undergo an increase in hardness beyond the point of grain growth, indicative of hardening outside of the regular HP relationship. A more detailed discussion of the hardening contributions common to all alloys follows in Section 3.4.

3.3. Calorimetry study

Adequate comparison of the performance of electrodeposited HEAs required a more thorough evaluation of their thermal stability than what was offered by discrete isochronal annealing tests alone. To this end, differential scanning calorimetry (DSC) was employed to gain greater insight into the annealing behaviour of the electrodeposited HEAs studied here. Not only can the critical and peak temperatures for phenomena causing microstructural changes be directly determined from the enthalpy release/absorption during heating, but through the modified Kissinger analysis [46], activation energies (Q) for such phenomena can also be elucidated. DSC profiles for the electrodeposited HEAs with amorphous structures contain two sets of peaks (Fig. 6a shows an exemplar set of scans for NiFeCoW), corresponding to grain growth (or nanograins nucleation) at intermediate temperatures (450–550 °C) and phase decomposition (formation of oxides and intermetallics as per the diffraction data in Fig. 2) at higher temperatures (650–750 °C).

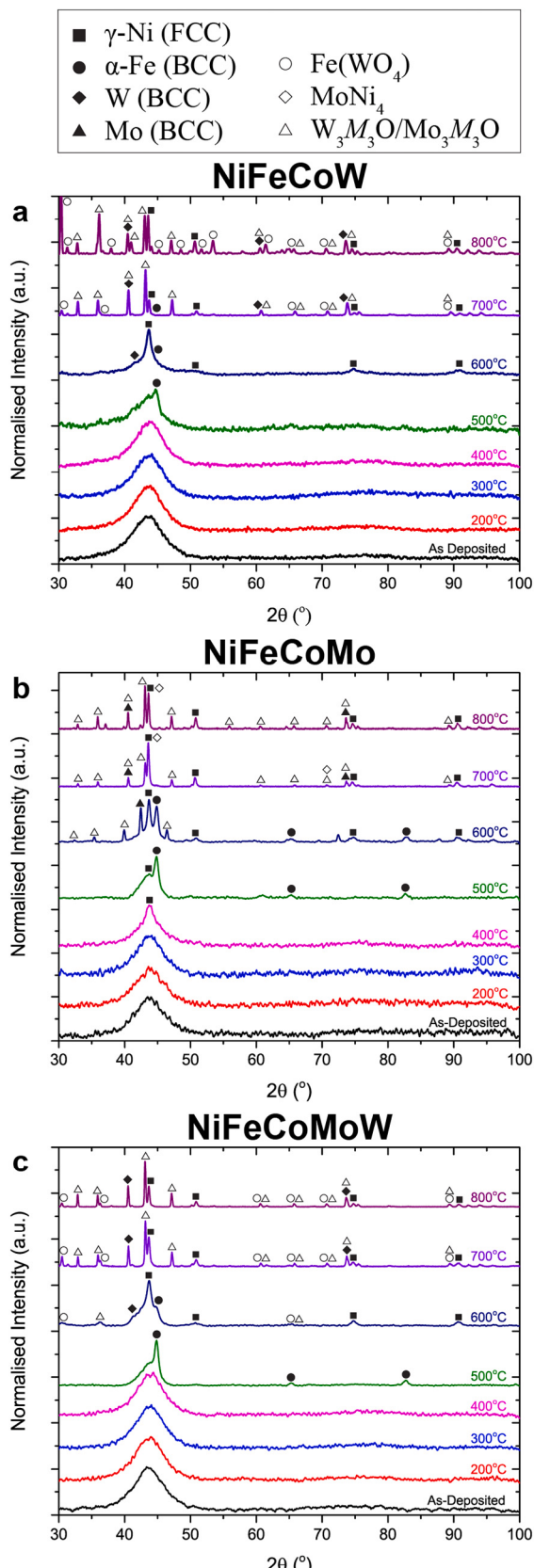


Fig. 2. Planar X-ray diffraction profiles of 1 h annealed (a) NiFeCoW (b) NiFeCoMo, and (c) NiFeCoMoW deposits.

Applying the modified Kissinger analysis to these datasets in Fig. 6b, activation energies for grain growth were determined from the slope of their respective linear fits.

Comparisons of the thermal stability of electrodeposited M/HEAs were made with alloy and pure metal subsets of [Ni-Fe-Co] in Table 3. The peak temperature for grain growth in these electrodeposited materials generally increased with their number of elements, making the largest jump of ~100 °C from 3-element (NiFeCo) to 4-elements (NiFeCoMo). The NiFeCoMoW, however, saw no improvement over NiFeCoMo, likely owing to limitations in its total Mo+W content (a result of restrictions in its synthesis, as discussed in further detail in ref. [38]). The activation energies for grain growth describe a clearer conclusion: Incremental increases were observed with each added element from pure metal to binary, ternary, and quaternary, reaching a maximum of 3.1 eV in NiFeCoW. The lower Q in NiFeCoMo compared to NiFeCoW is likely a result of its laminated structure. With the crystalline layers being depleted of Mo, the activation energy for their growth would likely be lower than that for the amorphous layers. The activation energy being of similar value to NiFe and NiFeCo (MEAs) is evidence of this. NiFeCoMoW having a slightly lower Q (2.9 eV) compared to NiFeCoW (3.1 eV) may be a result of limitations in achieving a perfectly equimolar alloy, with the total composition of Mo+W limited to ~25 at. %, as outlined in ref. [38].

Table 4 summarizes the activation energies for lattice self-diffusion (Q_v) and grain boundary diffusion (Q_{gb}) for diffusion couples made up of Ni, Fe, Co, Mo, and W. The activation energy for grain growth of equimolar NiFeCo is consistent with that of lattice self-diffusion for Ni, Fe, and Co, whereas in the pure metals (Ni and Co) it is comparatively low, on an order consistent with that of grain boundary self-diffusion of their respective elements. Considering the pure W and Mo diffusion couples, it would at first appear that the addition of one or both of these elements to the NiFeCo base forces a reversion back to grain-boundary diffusion, as the Q_v is far higher (4–6.6 eV) than the measure of activation volumes for grain growth in NiFeCo-(Mo/W) (2.3–3.1 eV). However, in considering binary couples with more dilute concentrations of Mo and W (which is more representative of the case of these electrodeposits), the measured data instead falls closer in line with the activation energies for self-diffusion, as observed in NiFeCo.

3.4. Strengthening mechanisms

The hardness (or strength) of a given material can be represented as the sum of contributions from the hardening mechanisms that it exhibits. One of the simplest formulations of this is:

$$H = H_o + H_{SS} + H_{GB} + H_{strain} + H_{precip} \quad (8)$$

where H_o is the friction stress contribution, H_{SS} solid-solution (SS) hardening, H_{GB} grain-boundary hardening, H_{strain} strain hardening, and H_{precip} precipitation hardening. In the low-temperature annealing regime (≤ 500 °C), characterized by limited grain growth/nucleation, the SS component is expected to be constant, as is the friction stress contribution. Here, the grain boundary hardening contribution is expected to dominate the mechanical behaviour of M/HEA electrodeposits, as they gradually develop from their initial nanocrystalline, amorphous, and nanoglass microstructures to coarser-grained, crystalline structures. This transition is modelled by the regular and inverse Hall-Petch effects described in the introduction and will be explored in Section 3.4.1.

3.4.1. Regular-to-inverse Hall-Petch transition

Grain boundary hardening is most commonly represented by the Hall-Petch effect, wherein the hardness of a material is proportional to the inverse-square-root of its grain size:

$$H = H_o + kd^{-1/2} \quad (9)$$

At some critical grain size (usually 10–25 nm), this relationship

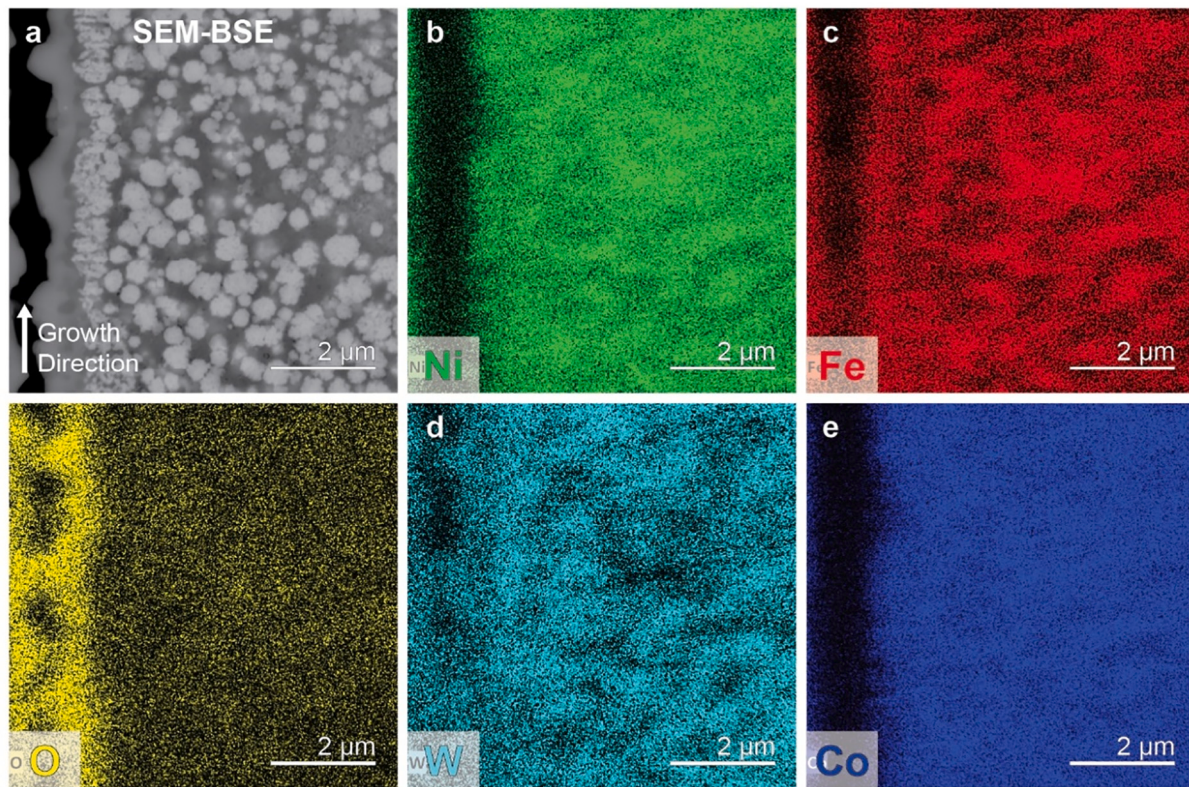


Fig. 3. Cross-sectional SEM-EDS maps of 700 °C annealed NiFeCoW. The arrow in (a) indicates the common growth direction for all micrographs. Note oxide formation on crack on the left side.

inverts itself, as hardness becomes directly proportional to grain size, generating the appropriately named inverse-Hall-Petch (IHP) relationship [61–63]. This transition from regular to inverse HP behaviour can manifest itself in two ways, first described by Kong et al. [52]: (i) extrinsically through post-fabrication processing and (ii) intrinsically in the as-fabricated state. That is, in the extrinsic transition grain sizes are varied through annealing treatments, whereas the intrinsic form, grain sizes are varied based on the fabrication parameters (such as varying the current density in electrodeposition). This has the effect that many studies on the intrinsic HP relationship in electrodeposited materials have required a change in deposit composition, which itself can alter the mechanical properties through SS hardening effects.

Fig. 7 shows the regular to inverse HP transition in each of the HEAs studied here (which are extrinsic), in comparison to literature data of extrinsic (Fig. 7a) and intrinsic (Fig. 7b) metals and alloys. Though lacking sufficient data points, the initially nanocrystalline NiFeCo alloy appears to behave similarly to the extrinsic NiCo and NiFeCoCrMn alloys, having a projected transition at ~30 nm, whereas Ni/NiFe in the intrinsic category (Fig. 7b) has transitions that occur at a finer grain size of ~12 nm. This shift in critical grain size has been assigned to alternative hardening mechanisms that arise from post-processing treatments, as grain boundary hardening also concerns itself with other grain boundary characteristics, such as grain boundary character (e.g., formation of special boundaries or disclination content), grain shape/morphology, and the state of grain boundaries (e.g., width, ordering, or segregation). Kong et al. [52,64] demonstrated in NiCo electrodeposits ($d = 18\text{--}23\text{ nm}$) that grain boundary relaxation dominates these contributing factors, as grains undergo recovery, rotation, and atomic reordering under low-temperature annealing ($\leq 225\text{ }^{\circ}\text{C}$), resulting in more ordered boundaries which are more resistant to transmission of slip. At finer starting grain sizes ($<10\text{ nm}$), this reordering is instead postulated to increase the stress required for grain-boundary mediated plasticity by reducing local stress concentrations [65].

The 4- and 5-element HEAs exhibit a behaviour more alike to the intrinsic NiP alloys, with a transition at very low grain sizes (5–10 nm). However, a significant difference in their trends is found in the wide spread of hardness at the finest of grain sizes ($>2\text{ nm}$) of the HEAs, which is postulated to be a result of the low-temperature annealing treatment undergone by those samples. In the work of Kong et al. [52,64], grain boundary relaxation was posited to control the entirety of the IHP region, as the starting grain size of their NiCo deposits was greater than what would be expected of an intrinsic HP-IHP transition. In this case, the 4- and 5-element alloys lie lower than the expected transition point, so while a grain boundary relaxation effect is expected, an intrinsic HP-IHP transition may also contribute to the trends observed in Fig. 7.

3.4.2. Grain boundary relaxation

One analytical method used to characterize grain boundary relaxation (GBR) is through the apparent activation volume for deformation (V), a measure of the characteristic volume over which work is done during a single thermally activated plastic event. This method has been outlined by Rupert et al. [65] in NiW electrodeposits annealed at temperatures 300 °C and below, where V/b^3 (activation volume normalized to the cube of the Burger's vector, b) has been shown to be larger in samples that undergo GBR hardening without measurable grain growth.

Nanoindentation strain-rate sensitivity tests were carried out on all near-equimolar HEA specimens. Activation volumes were then determined through the relationship in Eq. (3) of Section 2 and plotted as a function of annealing temperature up to 600 °C (Fig. 8), at which point significant phase decomposition occurs in the 4- and 5-element alloys (Section 3.1). Nanocrystalline NiCo [52] and NiFeCo [37] are also shown for comparison. At temperatures below the critical temperature for grain growth, the activation volume for NiCo ($d = 18\text{ nm}$) remains nearly unchanged, despite a rise in hardness of ~0.4 GPa (Fig. 7a) [37]. As summarized in Section 3.4.1, this rise in hardness is attributed to

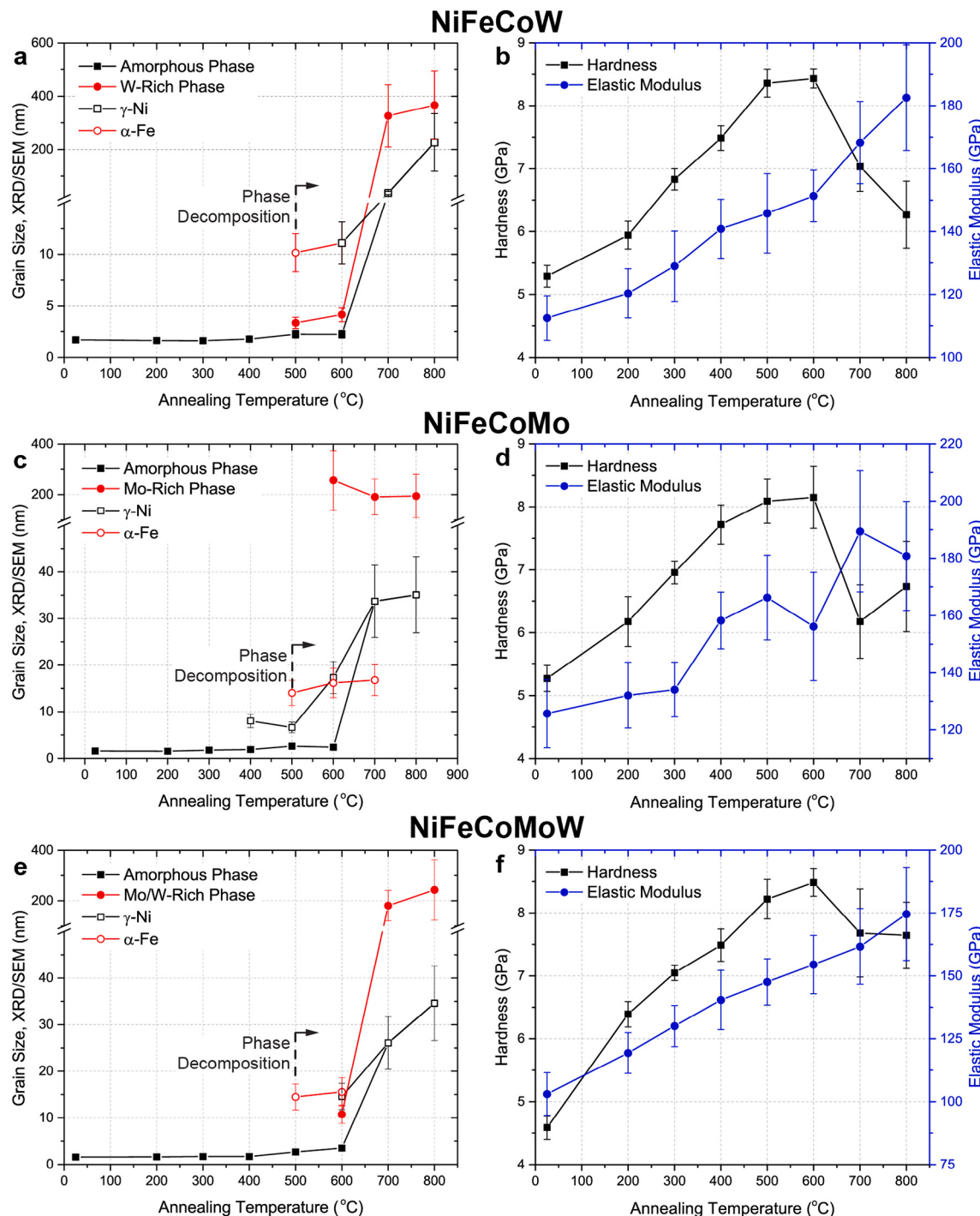


Fig. 4. (a, c) grain size (as measured by XRD/SEM) and (b, d) hardness and elastic modulus and as a function of annealing temperature in (a-b) NiFeCoW and (c-d) NiFeCoMo annealed for 1 h.

events such as grain recovery and rotation, and atomic reordering, resulting in grain boundaries that are more resistant to slip [64]. At higher annealing temperatures (>225 °C), there is a sudden increase in V , resulting from abnormal (225–300 °C) and normal (>300 °C) grain growth. In this material, it was established that grain boundary relaxation was responsible for the entirety of the IHP region [52].

NiFeCo, although similar in starting grain size, exhibits different behaviour; there is an immediate rise in V at 200 °C, followed by a drop at 300 °C, indicating that GBR in the form of increased stress requirements for grain-boundary mediated plasticity occurs at low temperature, but that its contribution to the inverse hardening trend is

largest at 200 °C. At 300 °C, the effects of GBR are more subdued, as IHP becomes the more dominant mechanism, the alloy experiencing more noticeable grain growth. At higher temperatures V then increases, coinciding with the larger interaction volumes present in coarse-grained structures, as the alloys fall back into the regular HP hardening regime.

NiFeCoW follows a similar trend as NiFeCo, an initial increase in V at 200 °C, followed by a decrease at 300 and 400 °C, then increasing due to nanocrystallization and grain growth at 500 °C and beyond. NiFeCoMo and NiFeCoMoW, exhibit nearly identical trends, each increasing incrementally at 200 and 300 °C, before dropping to a minimum at 400 °C. This indicates that the effect of relaxation is most prominent at

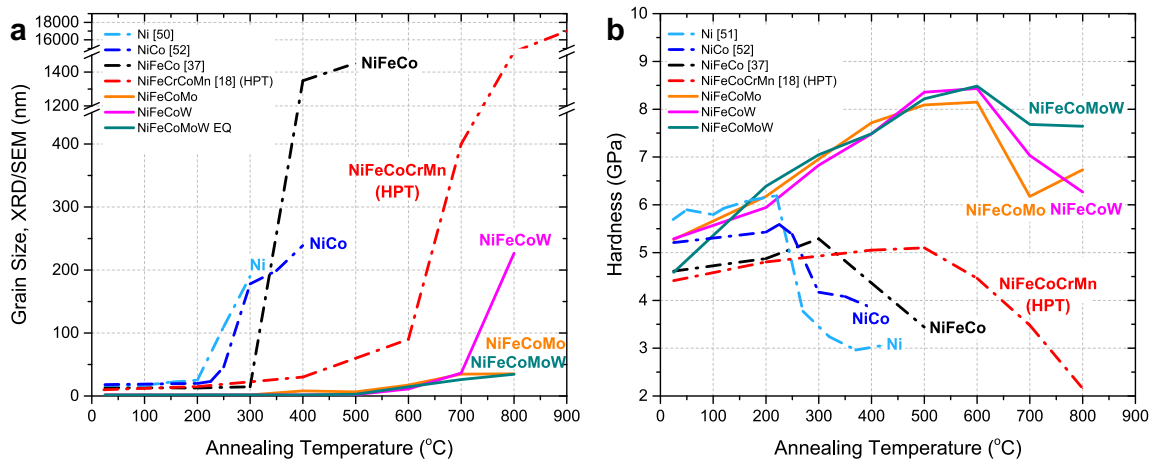


Fig. 5. (a) Grain size and (b) hardness as a function of annealing temperature for electrodeposited MEAs and HEAs annealed for 1 h. Electrodeposited Ni [50,51,], NiCo [52], NiFeCo [37] and NiFeCoCrMn [18] made by high-pressure torsion (HPT) are used as references.

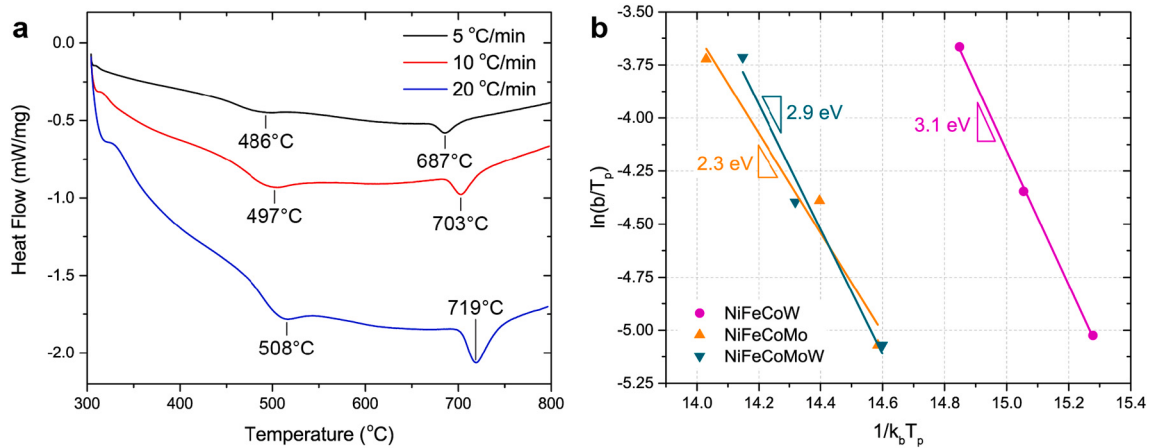


Fig. 6. (a) Exemplar DSC measurements for NiFeCoW at heating rates of 5, 10, and 20 °C·min⁻¹, with peak temperatures for grain growth and phase decomposition listed; and (b) fitting of the modified Kissinger analysis of the grain growth peak for near-equimolar NiFeCoW, NiFeCoMo, and NiFeCoMoW.

Table 3

Summary of DSC measurements and activation energies for grain growth from electrodeposited pure metals, binary alloys, and M/HEAs.

Alloy	As-deposited grain size (nm)	Scan rates (°C·min ⁻¹)	T _p - grain growth (°C)	T _p - phase decomposition (°C)	Q (eV)
NiFeCoMoW	Amorphous	5–20	522–547	697–723	2.9
NiFeCoMo	8	5–20	523–554	644–669	2.3
NiFeCoW	Amorphous	5–20	486–508	687–719	3.1
NiFeCo [37]	13	5–40	394–427	—	2.5
NiFe [54]	17	5–80	384–435	—	2.1
NiCo [55]	12	5–40	318–349	—	1.6
Co [56]	20	5–80	355–415	—	1.6
Ni [54]	46	5–80	272–329	—	1.3

300 °C in the alloys containing Mo, before the IHP begins to take over at 400 °C.

In the sub-10 nm grain size regime in which the 4- and 5-elements alloys exist, relaxation upon annealing has the effect of decreasing the density of local stress concentrations through annihilation of grain boundary defects, thus resulting in larger activation volumes for deformation to occur (translating to an increase in hardness) [65]. At first glance, the results in Fig. 8 therefore appear peculiar, as an overall increase in activation volume is expected with annealing when there is no change in the grain size of the alloy. NiFeCoMo follows this trend well, seeing a continuous rise in V up to the point of nanonucleation and grain growth (400 °C), likely owing to its dual amorphous/nanocrystalline

Table 4

Activation energies for lattice self-diffusion, Q_v, and grain boundary diffusion, Q_{gb}, for diffusion couples of Ni, Fe, Co, Mo, and W (formatted as M_p/M_i, where M_p is the parent metal/alloy, and M_i is the diffusing metal). All values were extracted from [57], unless otherwise indicated.

Diffusion couple	Q _v (eV)	Q _{gb} (eV)
Ni/Ni	2.7–3.0	1.2–1.9
Fe/Fe	2.6–2.9	1.0–1.9
Co/Co	2.0–2.5	1.2–1.5
Mo/Mo [58,59]	4.0–5.0	—
W/W	4.9–6.6	3.9
Ni-0.15%Co/Fe	2.559	2.291
Co-32%W/W	2.957	2.234
Ni-58.8%Mo/Ni [60]	2.879	—

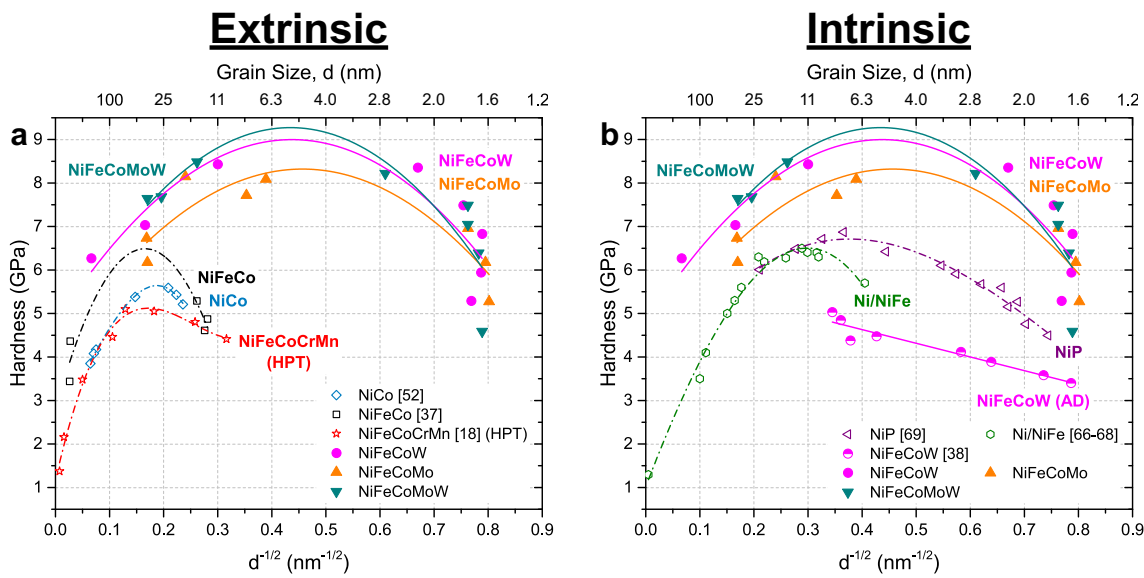


Fig. 7. Hall-Petch plots for near-equimolar NiFeCoW, NiFeCoMo, and NiFeCoMoW as compared to (a) extrinsic (NiCo [52], NiFeCo [37], NiFeCoCrMn [18]) and (b) intrinsic comparisons (Ni/NiFe [66–68], NiP [69], NiFeCoW [38]).

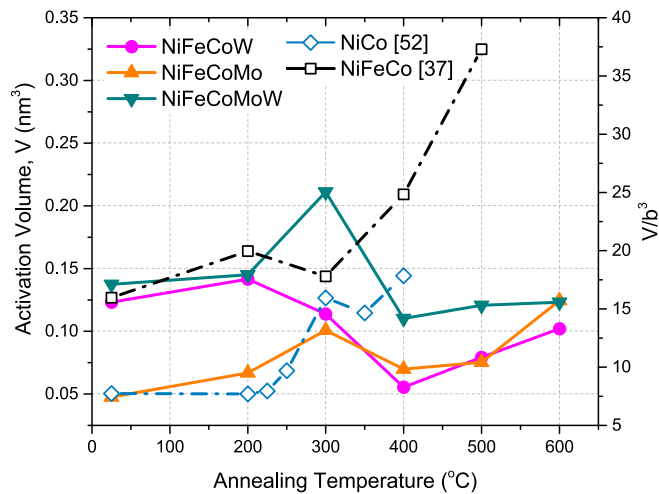


Fig. 8. Activation volume as a function of annealing temperature in near-equimolar electrodeposited HEAs. NiCo [52] NiFeCo [37] are listed as a comparison. NiCo is listed in terms of V/b^3 on the right axis, all others are simply plotted as V on the left axis.

nature. Whereas the more complex and more poorly understood nano-glass structures of NiFeCoW and NiFeCoMoW do not exhibit the same behaviour.

In amorphous metals and alloys, which contain no defined grains, plasticity is achieved through the generation/activation of shear transformation zones (STZs) [70]. These STZs are suspected to activate in regions of excess free volume, and therefore deformation is strongly dependent on local structure. Whereas in bulk metallic glasses (BMGs) the extent of local order varies randomly throughout the material, the excess volume contained within the interphase regions of nanoglasses (NGs) are approximately structurally comparable to shear bands [71,72]. In this way, NGs can undergo more homogenous deformation compared to BMGs owing to the activation of STZs along predefined boundaries [73]. This is expected to translate to a lower activation volume for NGs than BMGs or fully amorphous alloys, as activation of STZs would be more dependent on local structural defects in these materials. Thus, the trend observed in NiFeCoW takes on more meaning; (i) the initial increase in V from the as-deposited to the 200 °C annealed

state results from structural relaxation, as the amorphous domains and interphase regions reorganize to a lower energy state; (ii) a consecutive decrease in V at 300 °C and 400 °C resulting from a breakdown of the material's initial NG character, redistributing the excess free volume in the interphase regions throughout the regions of short-range order; and (iii) V increases with increasing temperature from 500 °C and upwards as a result nanograin nucleation and grain growth. Confirmation of such a sequence of microstructural changes is, however, necessary. This is investigated in further detail through Synchrotron XRD measurements in Section 3.4.3, which will also seek to address questions remaining regarding the evolution of activation volumes in NiFeCoMoW, and the balance of its control by its NG character and pronounced segregation of elements.

3.4.3. Synchrotron X-ray diffraction

Focusing on hardening in the low-temperature annealing regime that is postulated to be controlled by grain boundary relaxation, high-energy (65 keV) synchrotron XRD ($\lambda = 0.01905$ nm) was employed to elucidate more detailed structural information. The high resolution offered by high-energy X-rays and a large collection angle provides more insight into the fine changes that occurred in the samples over earlier conventional X-ray diffractometer measurements using a Cu source (Fig. 2), particularly in the amorphous-structured deposits.

Further insight into the short-range order (SRO) in these materials can be accomplished through pair distribution function (PDF) analysis, which is obtained by applying a Fourier transform to XRD data. The PDF, $G(r)$, describes the probability of finding an atom at a distance r from a reference atom [44]. From $G(r)$, abundant structural information can be discerned, such as coordination numbers (peak area), bond lengths (peak position), lattice disorder (peak width), and crystallite size (peak dampening) [45]. However, $G(r)$ naturally oscillates about zero, and as such is inconvenient for peak analysis beyond bond spacing. Another form of the PDF is known as the radial distribution function (RDF), calculated following Eq. (6) of Section 2, whose values are greater than zero which allows for easier peak fitting.

Applying this testing methodology to the 4- and 5-element alloys yielded the XRD and RDF profiles in Fig. 9. The XRD peak profiles remain largely unchanged in NiFeCoW (Fig. 9a) and NiFeCoMoW (Fig. 9e), aside from a slight strengthening of the (200) peak that becomes apparent at 400 °C, indicative of some early grain growth or strain relaxation processes taking place. More plainly seen in NiFeCoMo

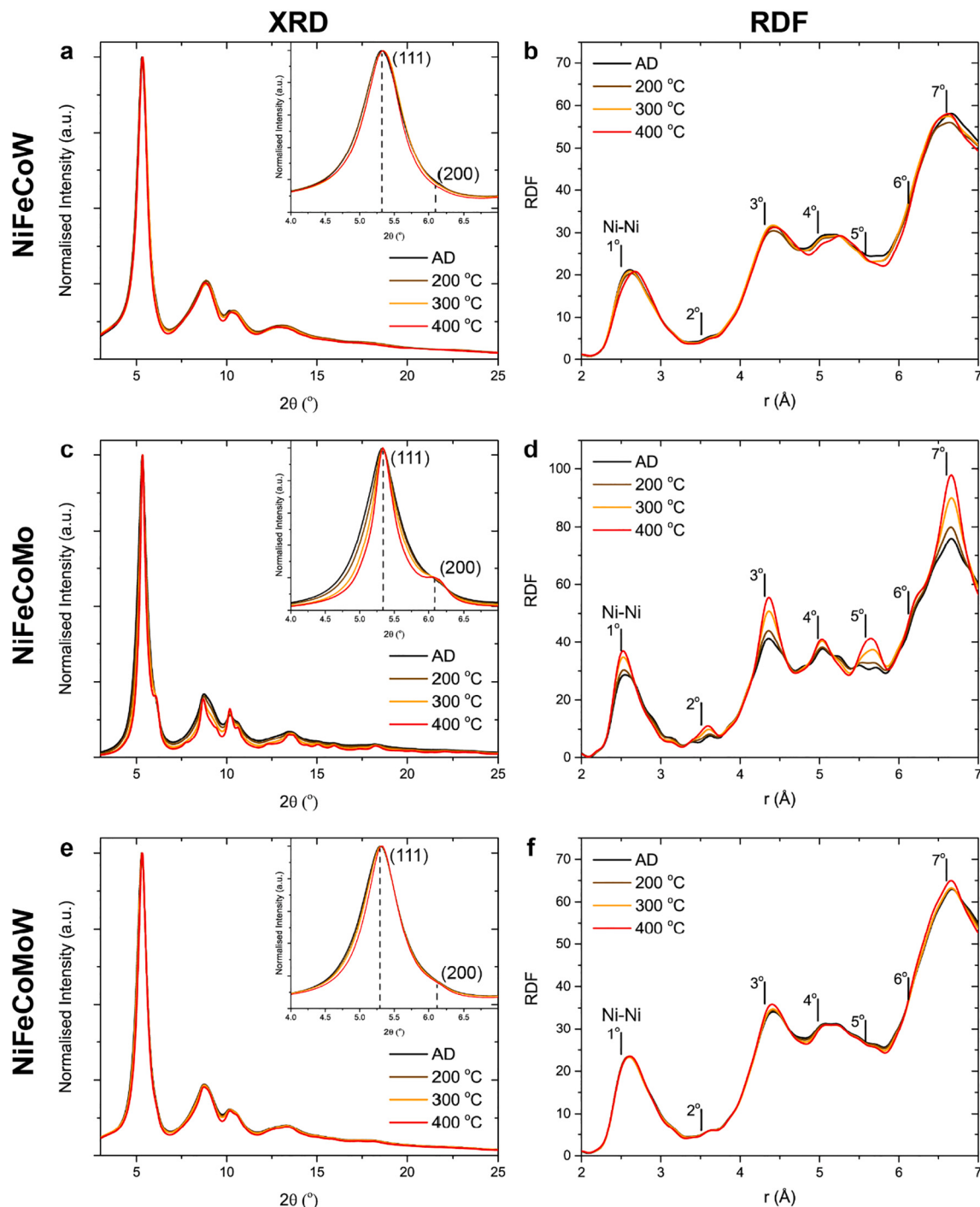


Fig. 9. Synchrotron XRD and RDF profiles of as-deposited (AD) and low-temperature annealed (≤ 400 °C) (a-b) NiFeCoW, (c-d) NiFeCoMo, and (e-f) NiFeCoMoW. The vertical lines in the RDF profiles indicate the first seven coordination positions for Ni–Ni bonding in a Ni reference sample.

(Fig. 9c) is sharpening of the (111) peak beginning at 200 °C, while the (200) emerges at 400 °C. This is likely a reflection of the differing energy barriers for grain-growth processes among the laminated layers in NiFeCoMo (Fig. 1b), as both crystallinity and composition play a role in this. Due to their largely amorphous nature, good fitting of the diffraction profiles could not be achieved for any of the three alloys, and therefore the more useful structural information lies in fitting of the RDF profiles (Fig. 9b, d, f). In these, a more severe upward shift is observed in the peak positions when compared to the pure Ni reference sample, owing to both the amorphous nature of the deposits and the introduction of W and/or Mo to the matrix. Minor changes in these profiles upon

annealing are again observed in NiFeCoW and NiFeCoMoW, which are more evident in larger coordination shells. NiFeCoMo experiences significant peak sharpening at each annealing temperature, with distinct peaks forming for each of the first seven coordination positions at 400 °C.

Gaussian fitting was performed on the peak corresponding to the first coordination position of each alloy for comparison, an exemplar of NiFeCoW shown in Fig. 10a. The shoulder that is apparent on the right of this first peak in each RDFs in Fig. 9 is likely reflective of the laminar segregation in the deposits: Ni with W in NiFeCoW and NiFeCoMoW; and Fe with Mo in NiFeCoMo (coupled with crystalline-amorphous

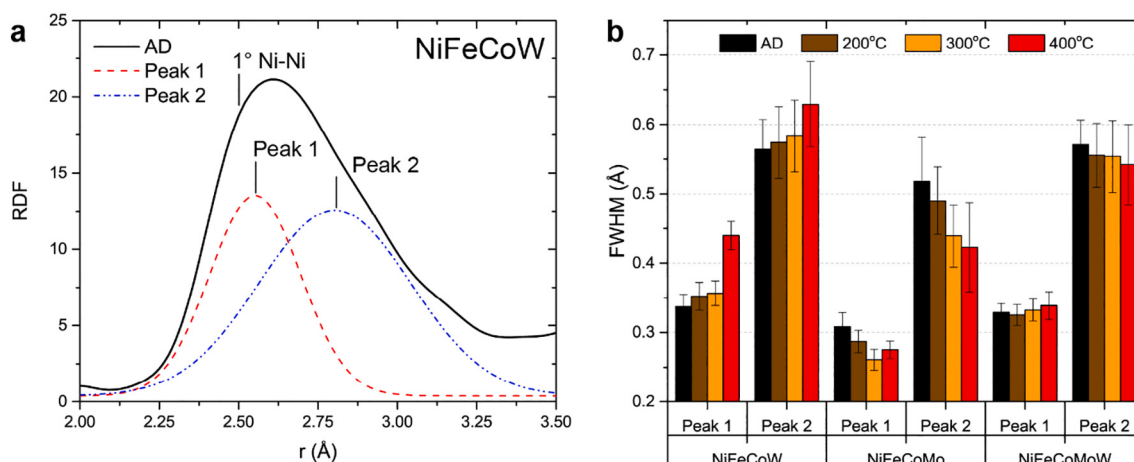


Fig. 10. (a) Exemplar RDF peak fit for as-deposited (AD) NiFeCoW, Peak 1 and Peak 2 reflective of the laminar nature of the deposits; and (b) FWHM of Peak 1 and Peak 2 in as-deposited and low-temperature annealed (≤ 400 °C, 1 h) NiFeCoW, NiFeCoMo, and NiFeCoMoW. The vertical line at $r = 2.5$ Å in (a) indicates the first coordination position (1°) for Ni–Ni bonding in a Ni reference sample.

layering), as shown in Ref. [38]. This shoulder may also reflect the nanoglass character of NiFeCoW and NiFeCoMoW, as the excess free volume of the interphase regions would increase the average bond distance among atoms. The FWHM of these two sets of peaks as a function of annealing temperature are shown in Fig. 10b. Of this dataset, only NiFeCoMo follows the expected trends, as peak widths decrease with increasing annealing temperature, indicating a lower degree of disorder at the atomic scale. NiFeCoMoW differs only in that its Peak 1 experiences almost no change with annealing, while Peak 2 follows the expected decreasing trend seen in NiFeCoMo. NiFeCoW is altogether dissimilar from both of these alloys, as both peaks become wider with increasing temperature. Accompanied with this is an upward shift in the peak centers, which may be indicative of homogenization of composition throughout the segregated layers in the alloy.

The defining differentiator between NGs and BMGs is enhanced ordering in NGs, seen in RDFs as sharpened peaks [74,75]. Therefore, the likely cause of peak broadening in NiFeCoW is attributed to a loss of its NG character upon low-temperature annealing, pushing it towards the purely amorphous scale with a lower degree of preferred nearest-neighbour distances. This aligns well with data from Section 3.4.2, which pointed to an evolution from NG to purely amorphous structure at annealing temperatures of 300 °C and 400 °C as the driving force for a decrease in activation volume (Fig. 8), which was most prominent at 400 °C.

The evolution of peak widths in NiFeCoMoW indicates a mixed response to annealing, as Peak 1 undergoes almost no change, while Peak 2 slightly decreases in width, seemingly appearing to be a near average of the responses seen in NiFeCoW and NiFeCoMo. The primary factor that separates this alloy from NiFeCoW is its more pronounced segregation of NiW [38]. Thus, these NiW-rich layers, associated with Peak 2, likely experience a relaxation, which would align with trends in activation volume (Fig. 8) in Section 3.4.2.

4. Conclusions

This work systematically examined the microstructural and mechanical stability of three types of electrodeposited nanostructured HEAs, as a study on the use of a viable synthesis route for potential HEA usage in high-performance applications. Improved grain size stability was observed with incremental additions of elements from Ni, NiCo, and NiFeCo, to the NiFeCoW and NiFeCoMo studied here. However, the final development stage of 5-element NiFeCoMoW saw no further improvement over its 4-element precursors, owing to limitations in compositional freedom of Mo and W due to intrinsic electroplating effects.

Calorimetric studies confirmed an overall improvement in thermal stability in electrodeposited HEAs over their binary and pure metal counterparts, represented as a doubling of the activation energy for grain growth in NiFeCoW (3.1 eV) and NiFeCoMoW (2.9 eV) compared to nanocrystalline Ni (1.3 eV).

Investigation of the mechanical behaviour of the electrodeposited HEAs revealed an extrinsic inverse-to-regular Hall-Petch transition upon nanocrystallization and grain coarsening, as well as the presence of grain boundary relaxation processes, leading to increases in hardness with no notable grain growth after low-temperature (<500 °C) annealing. With their performance in thermal stability and mechanical properties meeting, and even exceeding, the comparison of nanocrystalline NiFeCoCrMn made by HPT, electrodeposited nanostructured HEAs have here been established as promising candidate materials for future development in elevated temperature applications. Further, the process of electrodeposition itself shows great prospect to accelerate the commercial adoption of HEAs, which has thus far been limited. To this end, there are several evolutions of this work yet needed to accomplish such goals, including, but not limited to: (1) scaling of the electrodeposition processes to intermediate (2–5 L) and large (40–160 L) bath sizes, (2) standardized mechanical testing with use of scaled specimens, and (3) evaluation of functional properties such as magnetic, catalytic, electrical, adhesion, and wear behaviour.

CRediT authorship contribution statement

Michel J.R. Haché: Conceptualization, Data curation, Formal analysis, Investigation, Methodology, Writing – original draft, Writing – review & editing. **Yu Zou:** Funding acquisition, Supervision, Writing – review & editing. **Uwe Erb:** Funding acquisition, Supervision, Writing – review & editing.

Declaration of competing interest

The authors declare that they have no known competing financial interests or personal relationships that could have appeared to influence the work reported in this paper.

Data availability

Data will be made available on request.

Acknowledgements

Electron microscopy work was performed at the Open Centre for the Characterization of Advanced Materials (OCCAM), funded by the Canadian Foundation for Innovation. Synchrotron X-ray diffraction measurements were performed at the Canadian Light House (CLS) in Saskatoon, Canada. The authors thank Dr. Graham King at CLS for his assistance with synchrotron X-ray diffraction measurements. M.J.R.H. acknowledges financial support from Vanier Canada Graduate Scholarship (Natural Sciences and Engineering Research Council of Canada, NSERC) and the CLSI Student Travel Support Program. U.E. acknowledges financial support from NSERC, Discovery Grant #RGPIN-2016-055. Y.Z. acknowledges financial support from NSERC, Discovery Grant #RGPIN-2018-05731, Canada Foundation for Innovation (CFI)-John R. Evans Leaders Fund (JELF) Project# 38044, and Dean's Spark Assistant Professorship in the Faculty of Applied Science & Engineering at the University of Toronto.

Appendix A. Supplementary data

Supplementary data to this article can be found online at <https://doi.org/10.1016/j.surfcoat.2024.130719>.

References

- [1] E.O. Hall, The deformation and ageing of mild steel: III discussion of results, Proc. Phys. Soc. B 64 (1951) 747–753, <https://doi.org/10.1088/0370-1301/64/9/303>.
- [2] N.J. Petch, The cleavage strength of polycrystals, J. Iron Steel Inst. 174 (1953) 25–28.
- [3] R.W. Hertzberg, R.P. Vinci, J.L. Hertzberg, Deformation and Fracture Mechanics of Engineering Materials, 5th ed., John Wiley & Sons Inc., Hoboken, NJ, 2013.
- [4] J.-W. Yeh, S.-K. Chen, S.-J. Lin, J.-Y. Gan, T.-S. Chin, T.-T. Shun, C.-H. Tsau, S.-Y. Chang, Nanostructured high-entropy alloys with multiple principal elements: novel alloy design concepts and outcomes, Adv. Eng. Mater. 6 (2004) 299–303, <https://doi.org/10.1002/adem.200300567>.
- [5] B. Cantor, I.T.H. Chang, P. Knight, A.J.B. Vincent, Microstructural development in equiatomic multicomponent alloys, Mater. Sci. Eng. A 375–377 (2004) 213–218, <https://doi.org/10.1016/j.jmsea.2003.10.257>.
- [6] D.B. Miracle, O.N. Senkov, A critical review of high entropy alloys and related concepts, Acta Mater. 122 (2017) 448–511, <https://doi.org/10.1016/j.actamat.2016.08.081>.
- [7] E.P. George, R.O. Ritchie, High-entropy materials, MRS Bull. 47 (2022) 145–150, <https://doi.org/10.1557/s43577-022-00285-7>.
- [8] W. Li, D. Xie, D. Li, Y. Zhang, Y. Gao, P.K. Liaw, Mechanical behavior of high-entropy alloys, Prog. Mater. Sci. 118 (2021) 100777, <https://doi.org/10.1016/j.pmsci.2021.100777>.
- [9] H. Shahmir, T. Mousavi, J. He, Z. Lu, M. Kawasaki, T.G. Langdon, Microstructure and properties of a CoCrFeNiMn high-entropy alloy processed by equal-channel angular pressing, Mater. Sci. Eng. A 705 (2017) 411–419, <https://doi.org/10.1016/j.jmsea.2017.08.083>.
- [10] P. Sathiyamoorthi, J. Basu, S. Kashyap, K.G. Pradeep, R.S. Kottada, Thermal stability and grain boundary strengthening in ultrafine-grained CoCrFeNi high entropy alloy composite, Mater. Des. 134 (2017) 426–433, <https://doi.org/10.1016/j.matdes.2017.08.053>.
- [11] X. Yan, B. Zhu, Y. Zhang, S. Guo, H. Qiu, Phase formation and unusual interstitial solid-solution strengthening behavior of (CoCrFeMnNi)_x high-entropy ceramic films, Surf. Coat. Technol. 477 (2024) 130392, <https://doi.org/10.1016/j.surfcoat.2024.130392>.
- [12] C. Cheng, X. Zhang, M.J.R. Haché, Y. Zou, Magnetron co-sputtering synthesis and nanoindentation studies of nanocrystalline (TiZrHf)_x(NbTa)_{1-x} high-entropy alloy thin films, Nano Res. 15 (2022) 4873–4879, <https://doi.org/10.1007/s12274-021-3805-1>.
- [13] J. Wang, S. Wu, S. Fu, S. Liu, M. Yan, Q. Lai, S. Lan, H. Hahn, T. Feng, Ultrahigh hardness with exceptional thermal stability of a nanocrystalline CoCrFeNiMn high-entropy alloy prepared by inert gas condensation, Scr. Mater. 187 (2020) 335–339, <https://doi.org/10.1016/j.scriptamat.2020.06.042>.
- [14] M.J.R. Haché, C. Cheng, Y. Zou, Nanostructured high-entropy materials, J. Mater. Res. 35 (2020) 1051–1075, <https://doi.org/10.1557/jmr.2020.33>.
- [15] Y. Zou, J.M. Wheeler, H. Ma, P. Okle, R. Spolenak, Nanocrystalline high-entropy alloys: a new paradigm in high-temperature strength and stability, Nano Lett. 17 (2017) 1569–1574, <https://doi.org/10.1021/acs.nanolett.6b04716>.
- [16] Y. Zou, H. Ma, R. Spolenak, Ultrastrong ductile and stable high-entropy alloys at small scales, Nat. Commun. 6 (2015), <https://doi.org/10.1038/ncomms8748>.
- [17] B. Schuh, F. Mendez-Martin, B. Völker, E.P. George, H. Clemens, R. Pippan, A. Hohenwarter, Mechanical properties, microstructure and thermal stability of a nanocrystalline CoCrFeMnNi high-entropy alloy after severe plastic deformation, Acta Mater. 96 (2015) 258–268, <https://doi.org/10.1016/j.actamat.2015.06.025>.
- [18] H. Shahmir, J. He, Z. Lu, M. Kawasaki, T.G. Langdon, Effect of annealing on mechanical properties of a nanocrystalline CoCrFeNiMn high-entropy alloy processed by high-pressure torsion, Mater. Sci. Eng. A 676 (2016) 294–303, <https://doi.org/10.1016/j.jmsea.2016.08.118>.
- [19] T. Keil, S. Taheriniya, E. Bruder, G. Wilde, K. Durst, Effects of solutes on thermal stability, microstructure and mechanical properties in CrMnFeCoNi based alloys after high pressure torsion, Acta Mater. 227 (2022) 117689, <https://doi.org/10.1016/j.actamat.2022.117689>.
- [20] M. Vaidya, K. Guruvudiyathri, B.S. Murty, Phase formation and thermal stability of CoCrFeNi and CoCrFeMnNi equiatomic high entropy alloys, J. Alloys Compd. 774 (2019) 856–864, <https://doi.org/10.1016/j.jallcom.2018.09.342>.
- [21] P.T. Hung, M. Kawasaki, J.-K. Han, J.L. Lábár, J. Gubicza, Thermal stability of a nanocrystalline HfNbTiZr multi-principal element alloy processed by high-pressure torsion, Mater. Charact. 168 (2020) 110550, <https://doi.org/10.1016/j.matchar.2020.110550>.
- [22] Z. Wang, Z. Chen, Y. Fan, J. Shi, Y. Liu, X. Shi, J. Xu, Thermal stability of the multicomponent nanocrystalline Ni-ZrNbMoTa alloy, J. Alloys Compd. 862 (2021) 158326, <https://doi.org/10.1016/j.jallcom.2020.158326>.
- [23] C.C. Koch (Ed.), Nanostructured Materials: Processing, Properties, and Applications, 2nd ed., William Andrew Pub, Norwich, NY, 2007.
- [24] G. Bräuer, B. Szyszka, M. Vergöhl, R. Bandorf, Magnetron sputtering – milestones of 30 years, Vacuum 84 (2010) 1354–1359, <https://doi.org/10.1016/j.vacuum.2009.12.014>.
- [25] R.Z. Valiev, Producing bulk nanostructured metals and alloys by severe plastic deformation (SPD), in: S.H. Wang (Ed.), Nanostructured Metals and Alloys - Processing, Microstructure, Mechanical Properties, and Applications, Woodhead Publishing Ltd., Cambridge, UK, 2011, pp. 1–39.
- [26] C. Suryanarayana, E. Ivanov, V.V. Boldyrev, The science and technology of mechanical alloying, Mater. Sci. Eng. A 304–306 (2001) 151–158, [https://doi.org/10.1016/S0921-5093\(00\)01465-9](https://doi.org/10.1016/S0921-5093(00)01465-9).
- [27] D. Clark, D. Wood, U. Erb, Industrial applications of electrodeposited nanocrystals, Nanostruct. Mater. 9 (1997) 755–758, [https://doi.org/10.1016/S0965-9773\(97\)00163-3](https://doi.org/10.1016/S0965-9773(97)00163-3).
- [28] A. Robertson, U. Erb, G. Palumbo, Practical applications for electrodeposited nanocrystalline materials, Nanostruct. Mater. 12 (1999) 1035–1040, [https://doi.org/10.1016/S0965-9773\(99\)00294-9](https://doi.org/10.1016/S0965-9773(99)00294-9).
- [29] R. Parkinson, Electroforming — a unique metal fabrication process, NiDI Technical Series N 10 084 (1998) 15.
- [30] Z. Wang, J. Huo, X. Luan, S. Sun, G. Ma, Microstructure and electrochemical properties of FeCoNiCuZn high-entropy alloy films by DC electrodeposition, Int. J. Mater. Res. 113 (2022) 253–257, <https://doi.org/10.1515/ijmr-2021-8572>.
- [31] A. Aliyu, C. Srivastava, Phase constitution, surface chemistry and corrosion behavior of electrodeposited MnFeCoNiCu high entropy alloy-graphene oxide composite coatings, Surf. Coat. Technol. 429 (2022) 127943, <https://doi.org/10.1016/j.surfcoat.2021.127943>.
- [32] M. Dehestani, S. Sharafi, G.R. Khayati, The effect of pulse current density on the microstructure, magnetic, mechanical, and corrosion properties of high-entropy alloy coating Fe-Co-Ni-Mo-W, achieved through electro co-deposition, Intermetallics 147 (2022) 107610, <https://doi.org/10.1016/j.intermet.2022.107610>.
- [33] A.-M.J. Popescu, F. Branzoi, M. Burada, I. Atkinson, I. Constantin, J.C. Moreno, F. Miculescu, D. Mitrica, I.-C. Badea, M.T. Olaru, V. Constantin, Influence of heat treatment on the corrosion behavior of electrodeposited CoCrFeMnNi high-entropy alloy thin films, Coatings 12 (2022) 1108, <https://doi.org/10.3390/coatings12081108>.
- [34] S.-Q. Chang, C.-C. Cheng, P.-Y. Cheng, C.-L. Huang, S.-Y. Lu, Pulse electrodeposited FeCoNiMnW high entropy alloys as efficient and stable bifunctional electrocatalysts for acidic water splitting, Chem. Eng. J. 446 (2022) 137452, <https://doi.org/10.1016/j.cej.2022.137452>.
- [35] C.L.P. Pavithra, R.K.S.K. Janardhana, K.M. Reddy, C. Murapaka, J. Joardar, B. V. Sarada, R.R. Tamboli, Y. Hu, Y. Zhang, X. Wang, S.R. Dey, An advancement in the synthesis of unique soft magnetic CoCuFeNiZn high entropy alloy thin films, Sci. Rep. 11 (2021) 8836, <https://doi.org/10.1038/s41598-021-87786-8>.
- [36] M.J.R. Haché, Y. Zou, U. Erb, Post-deposition crack evolution in Cr(III) alloy electrodeposits: phenomenology, Surf. Coat. Technol. 406 (2021) 126648, <https://doi.org/10.1016/j.surfcoat.2020.126648>.
- [37] M.J.R. Haché, J. Tam, U. Erb, Y. Zou, Electrodeposited nanocrystalline medium-entropy alloys – an effective strategy of producing stronger and more stable nanomaterials, J. Alloys Compd. 899 (2022) 163233, <https://doi.org/10.1016/j.jallcom.2021.163233>.
- [38] M.J.R. Haché, J. Tam, U. Erb, Y. Zou, Electrodeposited NiFeCo-(Mo,W) high-entropy alloys with nanocrystalline and amorphous structures, J. Alloys Compd. 952 (2023) 170026, <https://doi.org/10.1016/j.jallcom.2023.170026>.
- [39] A.L. Patterson, The Scherrer formula for X-ray particle size determination, Phys. Rev. 56 (1939) 978–982, <https://doi.org/10.1103/PhysRev.56.978>.
- [40] ISO 14577-1: 2015, Metallic Materials - Instrumented Indentation Test for Hardness and Materials Parameters - Part 1: Test Method, International Organization for Standardization, 2015. <https://www.iso.org/obp/ui/#iso:std:iso:14577-1:ed-2:v1:en>.
- [41] W.D. Nix, H. Gao, Indentation size effects in crystalline materials: a law for strain gradient plasticity, J. Mech. Phys. Solids 46 (1998) 411–425, [https://doi.org/10.1016/S0022-5096\(97\)00086-0](https://doi.org/10.1016/S0022-5096(97)00086-0).
- [42] U.F. Kocks, A.S. Argon, M.F. Ashby, Thermodynamics and kinetics of slip, in: B. Chalmers, J.W. Christian, T.B. Massalski (Eds.), Progress in Materials Science, Pergamon Press, Oxford, 1975.

- [43] G. Taylor, Thermally-activated deformation of BCC metals and alloys, *Prog. Mater. Sci.* 36 (1992) 29–61, [https://doi.org/10.1016/0079-6425\(92\)90004-Q](https://doi.org/10.1016/0079-6425(92)90004-Q).
- [44] T. Proffen, S.J.L. Billinge, T. Egami, D. Louca, Structural analysis of complex materials using the atomic pair distribution function — a practical guide, *Z. Krist.* 218 (2003) 132–143, <https://doi.org/10.1524/zkri.218.2.132.20664>.
- [45] V. Petkov, Pair distribution functions analysis, in: E.N. Kaufmann (Ed.), *Characterization of Materials*, John Wiley & Sons, Inc., Hoboken, NJ, USA, 2012, p. com159, <https://doi.org/10.1002/0471266965.com159>.
- [46] L.C. Chen, F. Spaepen, Analysis of calorimetric measurements of grain growth, *J. Appl. Phys.* 69 (1991) 679–688, <https://doi.org/10.1063/1.347349>.
- [47] A. Mulone, A. Nicolenco, J. Fornell, E. Pellicer, N. Tsyntsaru, H. Cesilis, J. Sort, U. Klement, Enhanced mechanical properties and microstructural modifications in electrodeposited Fe-W alloys through controlled heat treatments, *Surf. Coat. Technol.* 350 (2018) 20–30, <https://doi.org/10.1016/j.surfcoat.2018.07.007>.
- [48] A. Mulone, A. Nicolenco, V. Hoffmann, U. Klement, N. Tsyntsaru, H. Cesilis, In-depth characterization of as-deposited and annealed Fe-W coatings electrodeposited from glycolate-citrate plating bath, *Electrochim. Acta* 261 (2018) 167–177, <https://doi.org/10.1016/j.electacta.2017.12.051>.
- [49] Y. Zhou, U. Erb, K.T. Aust, The role of interface volume fractions in the nanocrystalline to amorphous transition in fully dense materials, *Philos. Mag.* 87 (2007) 5749–5761, <https://doi.org/10.1080/14786430701716987>.
- [50] H. Natter, M. Schmelzer, R. Hempelmann, Nanocrystalline nickel and nickel-copper alloys: synthesis, characterization, and thermal stability, *J. Mater. Res.* 13 (1998) 1186–1197, <https://doi.org/10.1557/JMR.1998.0169>.
- [51] A. Torrents, H. Yang, F.A. Mohamed, Effect of annealing on hardness and the modulus of elasticity in bulk nanocrystalline nickel, *Metall. Mater. Trans. A* 41 (2010) 621–630, <https://doi.org/10.1007/s11661-009-0147-0>.
- [52] J. Kong, M.J.R. Haché, J. Tam, J.L. McCrea, J.Y. Howe, U. Erb, On the extrinsic Hall-Petch to inverse Hall-Petch transition in nanocrystalline Ni-Co electrodeposits, *Scr. Mater.* 218 (2022) 114799, <https://doi.org/10.1016/j.scriptamat.2022.114799>.
- [53] U. Klement, U. Erb, A.M. El-Sherik, K.T. Aust, Thermal stability of nanocrystalline Ni, *Mater. Sci. Eng. A* 203 (1995) 177–186, [https://doi.org/10.1016/0921-5093\(95\)09864-X](https://doi.org/10.1016/0921-5093(95)09864-X).
- [54] U. Klement, M. da Silva, G. Hibbard, Thermal stability of nanocrystalline Ni- and Co-based pulsed current electrodeposits: correlation of calorimetric measurements and microstructure development upon annealing, *Trans. IMF* 95 (2017) 20–24, <https://doi.org/10.1080/00202967.2017.1263475>.
- [55] G.D. Hibbard, K.T. Aust, U. Erb, Thermal stability of electrodeposited nanocrystalline Ni-Co alloys, *Mater. Sci. Eng. A* 433 (2006) 195–202, <https://doi.org/10.1016/j.msea.2006.06.096>.
- [56] G.D. Hibbard, K.T. Aust, U. Erb, The effect of starting nanostructure on the thermal stability of electrodeposited nanocrystalline Co, *Acta Mater.* 54 (2006) 2501–2510, <https://doi.org/10.1016/j.actamat.2006.01.028>.
- [57] I. Kaur, W. Gust, L. Kozma, *Handbook of Grain and Interphase Boundary Diffusion Data*, Ziegler Press, Stuttgart, 1989.
- [58] J. Askill, D.H. Tomlin, Self-diffusion in molybdenum, *Philos. Mag.* 8 (1963) 997–1001, <https://doi.org/10.1080/14786436308214459>.
- [59] K. Maier, H. Mehrer, G. Rein, Self-diffusion in molybdenum, *Int. J. Mater. Res.* 70 (1979) 271–276, <https://doi.org/10.1515/ijmr-1979-700412>.
- [60] G.P. Heijlegen, G.D. Rieck, Diffusion in the Mo-Ni, Mo-Fe and Mo-Co systems, *Acta Metall.* 22 (1974) 1269–1281, [https://doi.org/10.1016/0001-6160\(74\)90140-0](https://doi.org/10.1016/0001-6160(74)90140-0).
- [61] A.H. Chokshi, A. Rosen, J. Karch, H. Gleiter, On the validity of the Hall-Petch relationship in nanocrystalline materials, *Scr. Metall.* 23 (1989) 1679–1683, [https://doi.org/10.1016/0036-9748\(89\)90342-6](https://doi.org/10.1016/0036-9748(89)90342-6).
- [62] G. McMahon, U. Erb, Bulk amorphous and nanocrystalline Ni-P alloys by electroplating, *Microstruct. Sci.* 17 (1989) 447–457.
- [63] S.N. Naik, S.M. Walley, The Hall-Petch and inverse Hall-Petch relations and the hardness of nanocrystalline metals, *J. Mater. Sci.* 55 (2020) 2661–2681, <https://doi.org/10.1007/s10853-019-04160-w>.
- [64] J. Kong, T.J.H. Li, M.J.R. Haché, J. Tam, J.L. McCrea, J.Y. Howe, U. Erb, In situ annealing studies on the microstructural evolution of a macro defect free electroformed nanocrystalline Ni-Co sheet metal and its relation to tensile properties, *Acta Mater.* (2023) 118711, <https://doi.org/10.1016/j.actamat.2023.118711>.
- [65] T.J. Rupert, J.R. Trelewicz, C.A. Schuh, Grain boundary relaxation strengthening of nanocrystalline Ni-W alloys, *J. Mater. Res.* 27 (2012) 1285–1294, <https://doi.org/10.1517/jmr.2012.55>.
- [66] A.M. El-Sherik, U. Erb, G. Palumbo, K.T. Aust, Deviations from Hall-Petch behaviour in as-prepared nanocrystalline nickel, *Scr. Metall. Mater.* 27 (1992) 1185–1188, [https://doi.org/10.1016/0956-716X\(92\)90596-7](https://doi.org/10.1016/0956-716X(92)90596-7).
- [67] J.D. Giallonardo, U. Erb, K.T. Aust, G. Palumbo, The influence of grain size and texture on the Young's modulus of nanocrystalline nickel and nickel-iron alloys, *Philos. Mag.* 91 (2011) 4594–4605, <https://doi.org/10.1080/14786435.2011.615350>.
- [68] U. Erb, G. Palumbo, R. Zugic, K.T. Aust, Structure-property relationships for electrodeposited nanocrystals, in: *Processing and Properties of Nanocrystalline Materials*, TMS, Warrendale, PA, 1996, pp. 93–110.
- [69] G. Palumbo, U. Erb, K.T. Aust, Triple line dislocation effects on the mechanical behaviour of materials, *Scr. Metall. Mater.* 24 (1990) 2347–2350, [https://doi.org/10.1016/0956-716X\(90\)90091-T](https://doi.org/10.1016/0956-716X(90)90091-T).
- [70] C. Schuh, T. Hufnagel, U. Ramamurthy, Mechanical behavior of amorphous alloys, *Acta Mater.* 55 (2007) 4067–4109, <https://doi.org/10.1016/j.actamat.2007.01.052>.
- [71] Y. Ritter, D. Şopu, H. Gleiter, K. Albe, Structure, stability and mechanical properties of internal interfaces in Cu₆₄Zr₃₆ nanoglasses studied by MD simulations, *Acta Mater.* 59 (2011) 6588–6593, <https://doi.org/10.1016/j.actamat.2011.07.013>.
- [72] O. Franke, D. Leisen, H. Gleiter, H. Hahn, Thermal and plastic behavior of nanoglasses, *J. Mater. Res.* 29 (2014) 1210–1216, <https://doi.org/10.1557/jmr.2014.101>.
- [73] J.X. Fang, U. Vainio, W. Puff, R. Würschum, X.L. Wang, D. Wang, M. Ghafari, F. Jiang, J. Sun, H. Hahn, H. Gleiter, Atomic structure and structural stability of Sc₇₅Fe₂₅ nanoglasses, *Nano Lett.* 12 (2012) 458–463, <https://doi.org/10.1021/nl2038216>.
- [74] M. Ghafari, S. Kohara, H. Hahn, H. Gleiter, T. Feng, R. Witte, S. Kamali, Structural investigations of interfaces in Fe₉₀Sc₁₀ nanoglasses using high-energy X-ray diffraction, *Appl. Phys. Lett.* 100 (2012) 133111, <https://doi.org/10.1063/1.3699228>.
- [75] M. Ghafari, X. Mu, J. Bednarcik, W.D. Hutchison, H. Gleiter, S.J. Campbell, Magnetic properties of iron clusters in Sc₇₅Fe₂₅ nanoglass, *J. Magn. Magn. Mater.* 494 (2020) 165819, <https://doi.org/10.1016/j.jmmm.2019.165819>.